Electronic Supplementary Material (ESI) for Journal of Materials Chemistry C.
This journal is © The Royal Society of Chemistry 2020

Electronic Supplementary Information

Electrode-controlled confinement of conductive filaments in nanocolumn embedded symmetric-asymmetric RRAM structure

Wen Xiao,[a,b] *Wendong Song,*[*,a] *Yuan Ping Feng,*[c] *Daqiang Gao,*[b] *Yao Zhu,*[a] *Jun Ding*[*,b]

[*]Corresponding authors

[a]Institute of Microelectronics, Agency for Science, Technology and Research (A*STAR), 2 Fusionopolis Way, #08-02 Innovis, Singapore 138634, Singapore

E-mail: song_wen_dong@ime.a-star.edu.sg

[b]Department of Materials Science and Engineering, National University of Singapore, 9 Engineering Drive 1, Singapore 117575, Singapore

Email: msedingj@nus.edu.sg

[c]Department of Physics, National University of Singapore, 2 Science Drive 3, Singapore 117542, Singapore

Experimental

Synthesis

A ~50 nm Ta film was firstly deposited on $1\mu m$-SiO_2/Si substrate by sputtering. After that, a ~5 nm Fe_3O_4 nanocolumn film was assembled on the Ta film by pulsed laser deposition (PLD) at 300 ℃ under oxygen partial pressure of 5×10^{-6} Torr using laser energy of 250 mJ and high laser frequency of 10 Hz.[1] The Fe_3O_4 nanocolumn and Ta film form nanocolumn Fe_3O_4-Ta bottom electrode. After cooling down, a ~10 nm Ta_2O_5 film was further deposited at room temperature under oxygen partial pressure of 1 mTorr. The laser energy and deposition frequency were set to be 250 mJ and 5 Hz respectively. Then, a continuous Fe_3O_4 film was deposited through a shadow mask on top of the Ta_2O_5 film at 300 ℃ under oxygen partial pressure of 5×10^{-6} Torr with low laser frequency of 2 Hz. Finally, a Ru contact plug of ~20 nm in thickness was deposited through the shadow mask on top of the continuous Fe_3O_4 film by sputtering. The shape of the RRAM cell was round with a diameter of 100 μm determined by the shadow mask.

Characterizations

Thin film X-ray diffractometry (XRD; Bruker D8 Advance) with a Cu $K\alpha$ (1.5418 Å) source was employed to characterize the crystal structure of the Fe_3O_4 layer. Current-voltage (I-V) characteristics were measured using Keithley 2635B SourceMeter SMU Instrument with direct-current (dc) voltage sweeping mode. Temperature-dependent resistance (RT) measurements were taken using physical property measurement system (PPMS EverCool-II; Quantum Design). Constant-current mode with an excitation current of 0.1 μA was used for the RT measurements. Transmission electron microscopy (TEM; Tecnai G2 F20 X-TWIN at 200 kV) analyses were carried out to study the microstructures of the RRAM cell. Electron energy loss spectroscopy (EELS; Attachment of TEM) was used to analyze the elemental distribution of the RRAM cell. Cross-sectional TEM sample was prepared by focused ion beam milling (FIB; Defect Analyzer DA300).

First-principles calculations

Vienna ab initio simulation package (VASP) was used to perform first-principles calculations based on density functional theory (DFT).[2] Electron-ion interaction was modeled using projector augmented wave (PAW) potentials.[3] Exchange and correlation effects were approximated using generalized gradient approximation (GGA) with Perdew-Burke-Ernzerhof (PBE) functional for structural relaxation.[4, 5] It is noted that HSE06 functional was further applied for density of states (DOS) and electrostatic potential calculations.[6, 7] The effective on-site Coulomb and exchange parameters, U-J, were set to be 1.35 eV and 3.61 eV to describe the Coulomb and exchange interaction of Ta and Fe respectively.[8, 9] The cutoff energy was set at 400 eV for the plane-wave basis restriction in all calculations. K-points were sampled under Monkhorst-Pack scheme for the Brillouin-zone integration.[10] All atoms were fully relaxed until the acting forces were <0.02 eV/Å. A self-consistency accuracy of 10^{-4} eV was researched for electronic loops. The simulated lattice constants of an unstrained bulk λ-Ta_2O_5 unit cell are a = 6.24 Å, b = 7.35 Å and c = 3.83 Å.[11] The formation energies of interstitial oxygen (O_i) in neutral state were calculated using the following equation: $E_f^{O_i} = E_{tot}^{O_i} - E_{tot}^{0} - \mu_O$, where $E_{tot}^{O_i}$ is the total DFT energy of the supercell with an interstitial oxygen, E_{tot}^{0} is the total energy of the corresponding supercell without O_i, μ_O is the chemical potential of the O atom. The actual chemical potential μ_O depends on the surrounding environment, varying from O-rich to O-poor conditions. In O-rich condition, $\mu_O = \frac{1}{2}E_{O2}$, where E_{O2} is the total DFT energy of an isolated oxygen molecule in vacuum. In O-poor (Ta-rich) condition, $\mu_O = \frac{1}{5}[E_{Ta2O5} - 2E_{Ta}^{Metal}]$, where E_{Ta}^{Metal} is the DFT energy of per Ta atom in metallic tantalum. The μ_O in O-rich condition was taken as reference with its upper bound (O-rich) set at 0 eV. The condition sets the lower bound (O-poor) of μ_O to be -4.59 eV. The energy barriers for V_O migration in Ta_2O_5 were calculated by the nudged elastic band (NEB) method as implanted in VASP.[12] After relaxation of the NEB images, the maximum residual forces acting on all atoms were <0.02 eV/Å.

Amorphous Ta_2O_5 model was generated using melt quenching method by first-principles molecular dynamics as implemented in VASP. Firstly, the crystalline λ-Ta_2O_5 ($Ta_{32}O_{80}$) was melted at 6000 K for 9 ps and then cooled down to 300 K with a cooling rate of 4 K/3 fs. After that, the structure was equilibrated at 300 K for 9 ps. Finally, the obtained bulk amorphous $Ta_{32}O_{80}$ structure was fully relaxed until the acting forces on all atoms were <0.02 $eV/$Å. The mass density of bulk amorphous and crystalline Ta_2O_5 structure was kept the same (8.2 g/cm^3).[11] Fig. S1† shows atomic structure of the relaxed amorphous $Ta_{32}O_{80}$ (inset) and the corresponding total radical distribution functions. The characteristic bond lengths for interaction pairs of Ta-O, O-O and Ta-Ta agrees well with literature reports.[13, 14]

Interface models of vacuum/Ta_2O_5/Ta (001), vacuum/Ta_2O_5/Au (111) and vacuum/Ta_2O_5/Fe_3O_4 (111) were constructed by joining amorphous $Ta_{32}O_{80}$ and crystalline slabs of body-centered cubic (BCC) Ta (a = 3.32 Å), face-centered cubic (FCC) Au (a = 4.08 Å) and spinel Fe_3O_4 (a = 8.406 Å) respectively.[1, 15, 16] A vacuum slab of 10 nm was used in all interface models. Relaxed atomic structures of the three interfaces are shown in Fig. S2a-c†. Fig. S2d illustrates that the Fe_3O_4 electrode in our experimental RRAM device is textured in (111) orientation. Thus, the most stable Fe_3O_4 Fe_{tet1}-O_1-(111)

surface termination was used to build the interface model.[1, 17] The n-type Schottky barrier height at the interface was calculated by $\phi_B = E^{Ta2O5\_bulk}_{CBM} - E^{Electode\_bulk}_{F} + \Delta V$. $E^{Ta2O5\_bulk}_{CBM}$ and $E^{Elecrode\_bulk}_{F}$ are the conduction band edge of bulk amorphous Ta_2O_5 and Fermi level of bulk electrode material (Ta, Au or Fe_3O_4) respectively and are calculated with respect to the average electrostatic potential in the corresponding bulk supercell. ΔV is the potential step form at the Ta_2O_5/electrode (Ta, Au or Fe_3O_4) interface and is determined by the difference between macroscopic averages of electrostatic potential in the Ta_2O_5 and corresponding electrode's bulk-like regions of the interface model.[18]

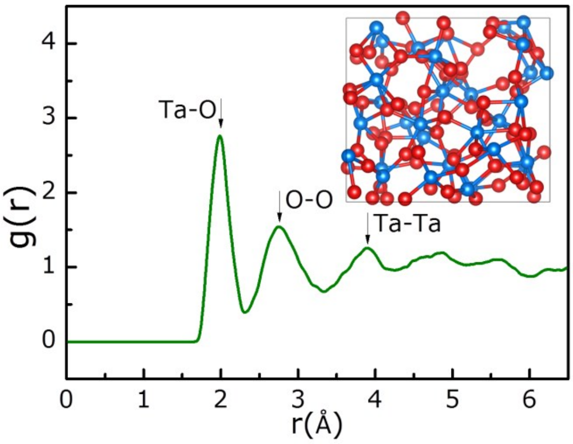

Fig. S1 Atomic structure of the relaxed amorphous $Ta_{32}O_{80}$ (inset) and the corresponding total radical distribution functions.

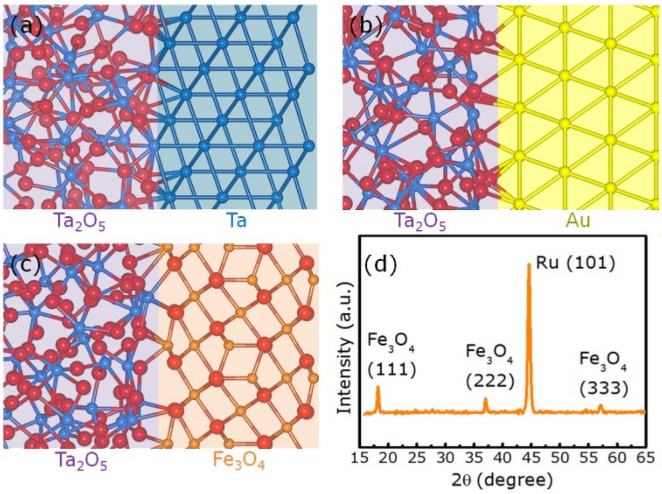

Fig. S2 Interfaces of (a) Ta_2O_5/Ta (001), (b) Ta_2O_5/Au (111) and (c) Ta_2O_5/Fe_3O_4 (111). (d) XRD spectrum of a nanocolumn Fe_3O_4/Ta_2O_5/Fe_3O_4-Ta RRAM cell with a top Ru contact plug.

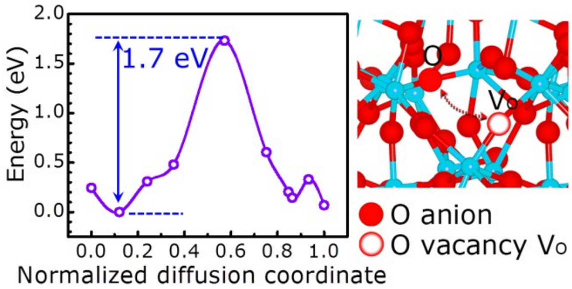

Fig. S3 Migration energy barrier and path of an oxygen vacancy (V_O) in amorphous Ta_2O_5.

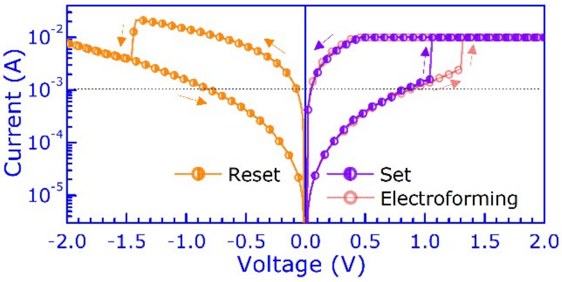

Fig. S4 Current-voltage (IV) characteristic of Fe_3O_4/Ta_2O_5 (15 nm)/Ta RRAM cell.

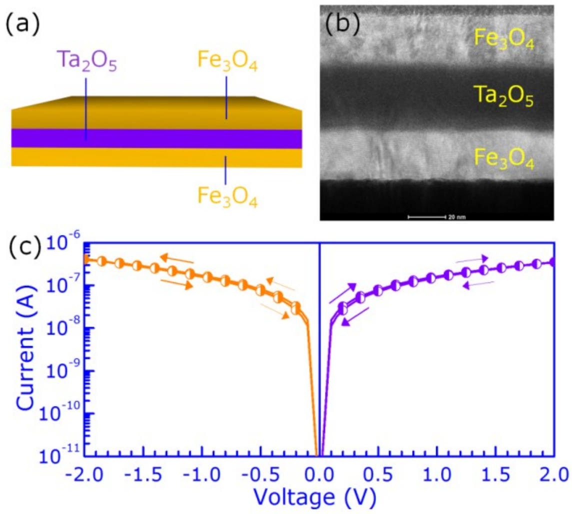

Fig. S5 (a) Schematic and (b) TEM image of a symmetric Fe_3O_4/Ta_2O_5/Fe_3O_4 architecture, and (c) the corresponding current-voltage (IV) characteristic.

A inert-inert electrode symmetric architecture is demonstrated using Fe_3O_4 as inert electrodes and Ta_2O_5 as resistive switching oxide. As shown in Fig. S5a-b, two continuous Fe_3O_4 electrode layers sandwich the Ta_2O_5 layer forming a symmetric $Fe_3O_4/Ta_2O_5/Fe_3O_4$ architecture. Current-voltage (IV) characteristic of the architecture in Fig. S5c shows that the resistance remains high (5×10^6 Ω) and unchanged with a small leakage current below 4×10^{-7} A, when applying a voltage ≤ 2 V with either positive or negative polarity. It indicates that no conduction path forms in the Ta_2O_5 sandwiched by two Fe_3O_4 inert electrodes and the symmetric architecture effectively blocks current flow.

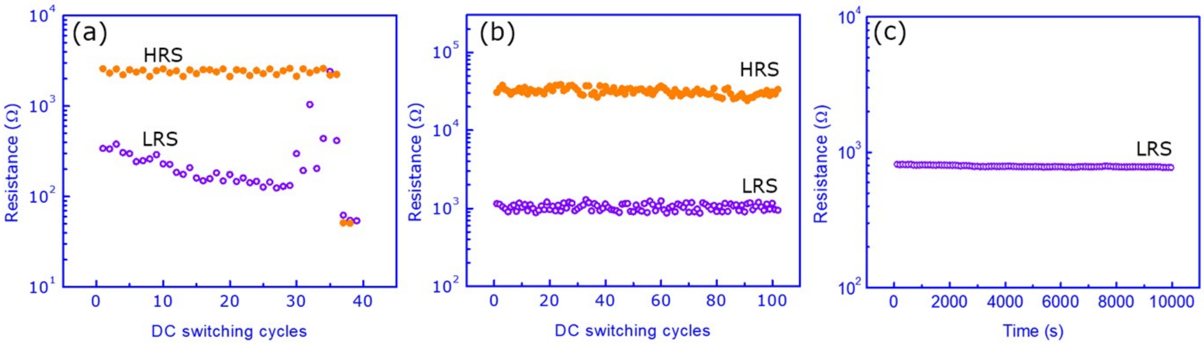

Fig. S6 Resistive switching endurance of (a) asymmetric Fe_3O_4/Ta_2O_5 (10 nm)/Ta and (b) nanocolumn symmetric-asymmetric $Fe_3O_4/Ta_2O_5/Fe_3O_4$-Ta RRAM cells. (c) Retention characteristic of the nanocolumn $Fe_3O_4/Ta_2O_5/Fe_3O_4$-Ta RRAM cell at room temperature.

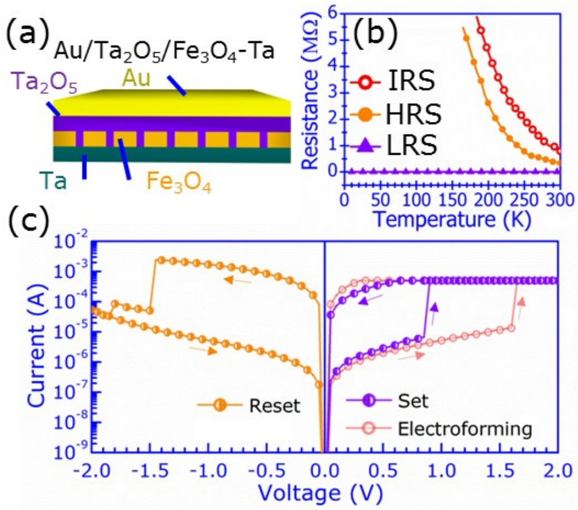

Fig. S7 (a) Schematic and (b) temperature-dependent resistance (RT) curves for the nanocolumn Au/Ta_2O_5/Fe_3O_4-Ta RRAM cell in IRS (red circle), HRS (orange dot) and LRS (purple triangle). (c) Current-voltage (IV) characteristic of the nanocolumn Au/Ta_2O_5/Fe_3O_4-Ta RRAM cell.

References

1. T. Herng, W. Xiao, S. Poh, F. He, R. Sutarto, X. Zhu, R. Li, X. Yin, C. Diao, Y. Yang, X. Huang, X. Yu, Y. Feng, A. Rusydi and J. Ding, *Nano Res.*, 2015, **8**, 2935-2945.
2. G. Kresse and J. Furthmüller, *Phys. Rev. B*, 1996, **54**, 11169-11186.
3. P. E. Blöchl, *Phys. Rev. B*, 1994, **50**, 17953-17979.
4. J. P. Perdew, J. A. Chevary, S. H. Vosko, K. A. Jackson, M. R. Pederson, D. J. Singh and C. Fiolhais, *Phys. Rev. B*, 1992, **46**, 6671-6687.
5. J. P. Perdew, K. Burke and M. Ernzerhof, *Phys. Rev. Lett.*, 1996, **77**, 3865-3868.
6. J. Heyd, G. E. Scuseria and M. Ernzerhof, *J. Chem. Phys.*, 2003, **118**, 8207-8215.
7. J. Heyd, J. E. Peralta, G. E. Scuseria and R. L. Martin, *J. Chem. Phys.*, 2005, **123**, 174101.
8. M. Cococcioni and S. de Gironcoli, *Phys. Rev. B*, 2005, **71**, 035105.
9. M. V. Ivanov, T. V. Perevalov, V. S. Aliev, V. A. Gritsenko and V. V. Kaichev, *J. Appl. Phys.*, 2011, **110**, 024115.
10. H. J. Monkhorst and J. D. Pack, *Phys. Rev. B*, 1976, **13**, 5188-5192.
11. S.-H. Lee, J. Kim, S.-J. Kim, S. Kim and G.-S. Park, *Phys. Rev. Lett.*, 2013, **110**, 235502.
12. H. Jónsson, G. Mills and K. W. Jacobsen, 1998.
13. Y.-N. Wu, L. Li and H.-P. Cheng, *Phys. Rev. B*, 2011, **83**, 144105.
14. R. Bassiri, K. Borisenko, D. Cockayne, J. Hough, I. MacLaren and S. Rowan, *Appl. Phys. Lett.*, 2011, **98**, 031904.
15. R. J. Bondi and M. J. Marinella, *J. Appl. Phys.*, 2015, **117**, 085308.
16. R. M. Fleming, D. V. Lang, C. D. W. Jones, M. L. Steigerwald, D. W. Murphy, G. B. Alers, Y.-H. Wong, R. B. van Dover, J. R. Kwo and A. M. Sergent, *J. Appl. Phys.*, 2000, **88**, 850-862.
17. M. E. Grillo, M. W. Finnis and W. Ranke, *Phys. Rev. B*, 2008, **77**, 075407.
18. D. Demchenko and A. Y. Liu, *Phys. Rev. B*, 2006, **73**, 115332.